ACS APPLIED NANO MATERIALS

www.acsanm.org Article

DNA Origami Chromophore Scaffold Exploiting HomoFRET Energy Transport to Create Molecular Photonic Wires

William P. Klein, Brian S. Rolczynski, Sean M. Oliver, Reza Zadegan, Susan Buckhout-White, Mario G. Ancona, Paul D. Cunningham, Joseph S. Melinger, Patrick M. Vora, Wan Kuang, Igor L. Medintz,* and Sebastián A. Díaz*

Cite This: *ACS Appl. Nano Mater.* 2020, 3, 3323−3336 Read Online

ACCESS | Metrics & More | Article Recommendations | Supporting Information

ABSTRACT: DNA-scaffolded molecular photonic wires (MPWs) displaying prearranged donor−acceptor chromophore pairs that engage in extended Förster resonance energy transfer (FRET) cascades represent an emerging nanoscale photonic material with numerous potential applications in data storage, encryption, and communications. For translation to such applications, these devices must first demonstrate robust performance with high transfer efficiencies over extended distances. Here, we report the optimization of FRET in a 6-helix DNA origami architecture supporting a 14-dye site system that contains a central 10-dye homogeneous FRET (HomoFRET) relay span and overall extends over 29 nm in length. Varying the dye density by controlling their presence or absence across all of the individually addressable sites presented an incredibly large optimization space (1024 HomoFRET and 16 384 total permutations). High-throughput experiments, with over 500 measurements of DNA templates assembled in parallel, allowed for the study of HomoFRET transfer as a function of fluorophore density and arrangement. Transfer within solution-phase MPWs initially obtained with steady-state spectroscopy experiments revealed values only reaching ∼1% efficiency. Extensive photophysical characterization, utilizing six different spectroscopic techniques and 11 total methodologies, determined that the diminished FRET efficiency of each individual component step is the principal cause of the limited transfer in solution. Monte Carlo and machine-learning methods provided additional insights into design optimization. A representative MPW set selected based on the previous findings was subsequently characterized in film deposition and also under cryogenic conditions. Under these improved conditions, selected MPWs demonstrated 59 ± 6% energy transport efficiency over a length of 29 nm; this is ∼25% longer and 10-fold more efficient than the previously reported optimized DNA MPWs.

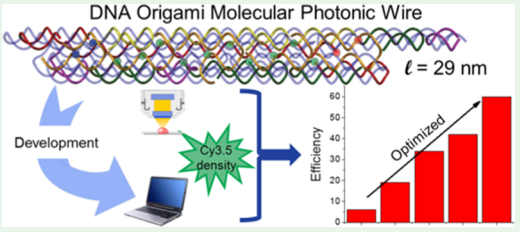

KEYWORDS: *molecular photonic wires, DNA nanotechnology, DNA origami, energy transfer, homogenous FRET, machine learning*

INTRODUCTION

As a molecular template for nanotechnology, DNA remains unrivaled for its versatility in design and its ease of use.[1] One area of promising application is that of excitonic/electronic energy transport,[2] which is central to many biophysical processes, and could be a basis for valuable future technologies such as light harvesting[3,4] and DNA data storage/encryption.[5−7] In this usage, DNA offers many advantages as a scaffolding molecule including biocompatibility,[8] low cost, stability,[9,10] a flexible design space in two dimensions (2-D) and three dimensions (3-D),[11−14] precise subnanometer positioning,[15,16] ease of functionalization (*e.g.*, with nanoparticles, dyes, enzymes, reaction reagents, *etc.*),[17−21] and open-access design tools.[22,23] DNA-organized dye networks are also highly modular and provide a nearly limitless search space for finding optimal dye configurations for energy transport.[4,24,25] The present study explores Förster resonance energy transport (FRET) within DNA-organized chromophore networks.[26]

The specific design of interest in this study was the molecular photonic wire (MPW).[2,27] Photonic wires are analogous to optical waveguides in the sense that light energy is transferred linearly from one end to the other. The most common strategy is to use organic dyes with energy propagation mediated by FRET.[28] When energy is transferred between two fluorophores of different types, the transfer is termed heterogeneous FRET, with the energy flowing "downhill" according to the respective absorption and emission frequencies of the acceptor and donor.[26] In homotransfer (HomoFRET), the energy transfer is instead between identical dyes, and this means there is no red-shift in the emission spectra due to energy loss at each dye, *i.e.*, the donor and acceptor wavelengths are essentially identical. HomoFRET has been shown to bridge between an input and

Received: January 8, 2020
Accepted: March 6, 2020
Published: March 23, 2020

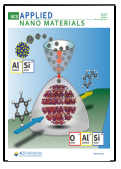

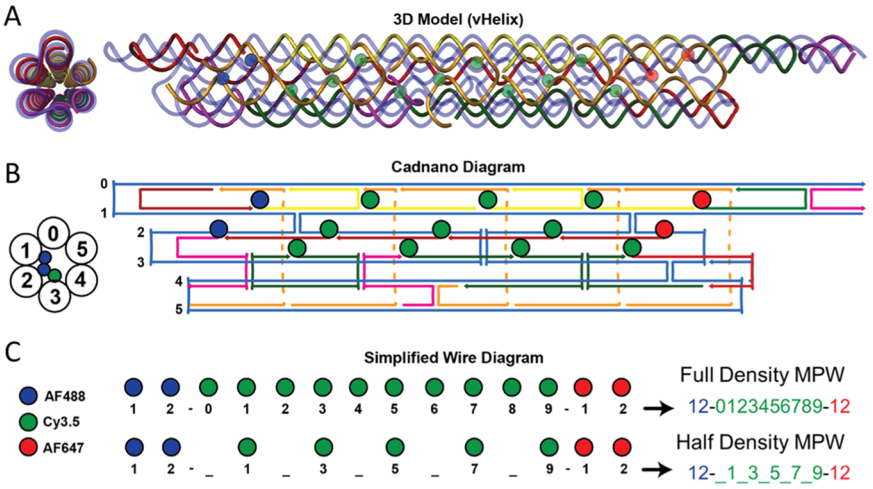

Figure 1. Schematics of DNA origami MPW. (A) vHelix model showing the 6-helix arrangement and the interior cavity.[22] (B) CaDNAno staple layout.[23] All dyes were bound to helix 1, 2, or 3. (C) Naming convention for MPWs. Dashes, "-", represent the boundary between the AF488, Cy3.5, and AF647 domains; a number represents that the respective dye position was present; and an underscore dash, "_", indicates that the unlabeled strand was used.

output hetero FRET step and effectively increase the distance over which MPWs become possible.[29−31] At the same time, the thermodynamic directional preference is lost in HomoFRET. HomoFRET will follow a random-walk path with back-energy transfer between dyes, resulting in quantum efficiency degradation in linear systems.[32,33] This differs from light-harvesting systems where centrosymmetric HomoFRET systems found neutral or increased transfer.[3,4,18] In a recent investigation of MPWs 24 nm in length, which included a long HomoFRET section, the end-to-end efficiencies were observed to be just 6% in poly(vinyl alcohol) (PVA) films,[34] and for similar solution-based MPWs of 30 nm in length, the reported efficiency was 1.7%.[30] From these published works, we developed a hypothesis that HomoFRET would benefit from creating greater density transfer networks by integrating as many dyes as possible. Increasing dye density results in more transfer steps, which would decrease the MPW efficiency; on the other hand, increased density should increase the efficiency of each step. At high FRET efficiencies, the increase should result in a faster growth of the average available steps, surmounting the negative effect of higher step requirements, leading to overall more efficient MPWs. To test this hypothesis, we required a more complex DNA scaffold that can accommodate many more dyes.[35] Specifically, we employed a 6-helix bundle DNA origami[36] that extends over 42 nm in length and contains a two-dye donor segment, a 10-dye homogeneous bridge or relay segment, and a two-dye acceptor segment. These segments were composed of repeating Alexa Fluor 488 (AF488), Cyanine 3.5 (Cy3.5), and Alexa Fluor 647 (AF647), respectively. Figure 1 shows a two-dimensional depiction of the three-dimensional vHelix model as well as the scaffold and staple routing of the wire depicting the fluorophore attachment locations adapted from CaDNAno software.[23] The blue, green, and red dots represent the AF488, Cy3.5, and AF647 attachment locations, respectively. This DNA origami MPW allowed us to create a HomoFRET relay section with varying densities as well as with individually addressable sites allowing for a large optimization space. Quantitatively, the structure could have up to 16384 distinct designs of the entire MPW and 1024 different configurations of the HomoFRET relay itself based on different permutations of including or not a chosen dye position.

The optimization of such an MPW would be straightforward if it were assumed that one could position the dyes at any location with precision, that the dye orientations were all controlled, and that the system was always governed by the Förster theory.[37] In this ideal scenario, the optimum design would simply be a very dense linear arrangement of the dyes.[30] However, in reality, the upper limits for transport efficiency in a DNA-scaffolded chromophore system will depend on factors such as the motion of the chromophores within the scaffold[30] and the spatial or electronic influences of the chromophores upon each other.[38,39] A balance must be achieved between the effects of increased dipole−dipole coupling, dye-quenching of dyes in close proximity, and external environmental influences that modify the optical properties of the dyes. Therefore, to use complex DNA-based systems such as these, we must develop efficient methods to understand the vast search space, find optimal sample configurations, and characterize them. We must understand whether these ideal limits are reached in realistic systems and how to remove the inhibiting bottlenecks. Finally, we must be able to distinguish multifaceted effects influencing the FRET efficiency. For these reasons, as will be presented, optimization of a DNA-scaffolded exciton network (we note that we refer to molecular excitons throughout the text) requires an empirical undertaking as well as theory-based optimization.

Using the large origami MPW sample library, we employed multiple methodologies to characterize and understand the MPW's design principles that would lead to optimal transfer. We used analytical models to identify the upper limit of energy transport efficiency for "ideal" systems with expected photophysical conditions (*i.e.*, perfect formation effectiveness, dye positioning, and meeting FRET assumptions). Comparing these predictions with the results of steady-state spectroscopy experiments, we found substantial discrepancies. Expanded characterization such as single-particle FRET (spFRET), lifetime fluorescence, and lifetime anisotropy provided insights into where the reality differed from the predicted parameters. Using the large data set obtained in the steady-state measurements (~150 different configurations and over 500 individual measurements) also allowed us to utilize machine-learning regression techniques to find a best fit to the entire data set and identify bottlenecks. We then created and assembled a small

https://dx.doi.org/10.1021/acsanm.0c00038
ACS Appl. Nano Mater. 2020, 3, 3323−3336

number of candidates from the large search space that would be of particular interest to characterize in thin-film deposition and cryogenic temperatures. In these conditions, we found large enhancements in transfer efficiency and much better agreement with the ideal predictions.

This report demonstrates how high-throughput parallel experiments afforded by DNA templates allow for the investigation of parameters with more subtle effects.[40] The results support the hypothesis that greater dye density results in optimized transfer, though the increase was less than predicted. After extensive characterization, we report MPWs of 29 nm in length that in PVA films have up to 59 ± 6% efficiency, or ∼25% longer and 10-fold more efficient than the highest values reported in the literature.[34]

RESULTS AND DISCUSSION

The primary aim of this project was to obtain the MPW with the greatest energy transfer efficiency by balancing dye density and HomoFRET processes. We constructed multiple permutations of our 6-helix bundle DNA origami, resulting in 29 nm long MPWs of differing dye densities. We tested 147 different MPWs, generally working in parallel preparations of 10−20 different permutations and utilizing the information obtained from one series of experiments to design the next series of MPWs to be tested. We first present a discussion of the characterization properties or figures of merit and a discussion of the models on which our density hypotheses were based. We then discuss the experimental characterization of the MPWs in the solution phase. Subsequently, we discuss computational analysis and any variation observed between the models and experimental results. In a final step, the experimental determination of a chosen subset of MPWs in film conditions is presented. The film conditions resulted in the highest transfer efficiencies, as compared to the solution values.

Figures of Merit. The MPW transfer efficiency is characterized by the number of photons emitted by the output, *i.e.*, terminal dye, as a function of excitons put into the MPWs through absorption of photons by the input dyes. We excite the structures at blue wavelength (λ_B) of 455 or 466 nm (the two wavelengths correspond to whether we are using the spectroscopy or microscopy setup; see the Materials and Methods section) to maximize the input excitation and minimize the direct excitation of downstream dyes. The overall measure of MPW efficiency is referred to as the end-to-end transfer efficiency (E_{ee}). The E_{ee} requires a correction factor to downstream excitation.[29,34] In the past, this has been accomplished with semianalytical methods that measured individual FRET efficiencies and respective extinction coefficients;[30] this methodology works well for simple structures. A purely experimental strategy in which control structures without the initial donor input dye (AF488) are measured can be undertaken; however, this methodology is very labor and material intensive.[18,29] For our current system, we exploited multiwavelength excitations, specifically adding a green 532 or 585 nm excitation wavelength (λ_G) that only excites the downstream (relay and acceptor) dyes and utilized a correction factor determined experimentally using control structures with no AF488. The two wavelengths again correspond to the microscopy or spectroscopy setup, respectively. This methodology has the advantages of being inexpensive in labor and material costs, but more importantly, efficiency determinations are independent of fluctuations in concentration.[41] Although the MPWs were generally at the same final concentration (∼10 nM), there are subtle differences in the origami formation efficiency as well as the purification steps that can cause miscalculations and add uncertainty. The final reported E_{ee} is given by eqs 1 and 2

$$E_{ee} = \left(\frac{\Phi^{\lambda_B,T}_{AF647} - (f \times \Phi^{\lambda_G,T}_{AF647})}{QY^{T}_{AF647}} \Big/ \frac{\Phi^{\lambda_B,T}_{AF488}}{QY^{T}_{AF488}} \right) \tag{1}$$

$$f = \frac{\Phi'^{\lambda_B,T}_{AF647}}{\Phi'^{\lambda_G,T}_{AF647}} \quad (\Phi' \text{ signifies the MPWs have no AF488}) \tag{2}$$

The $\Phi^{\lambda,T}_{AF647}$ are the photon counts emitted by the AF647 in an MPW excited at either the blue wavelengths (λ_B) or the green wavelength (λ_G) at a temperature T (in Kelvin). Solution-based measurements were realized only at room temperature, with PVA film characterization realized at 300 K and in cryo conditions at 5 K. QY are the fluorescence quantum yields of the respective dyes at T, and $\Phi^{\lambda_B,T}_{AF488}$ is the photon count from a DNA nanostructure that contains only the two AF488 at T.

An additional parameter that we call the wire transfer efficiency (WTE) has a similar profile as the E_{ee} but accounts for the variation in energy transfer from the donors into the Cy3.5 HomoFRET relay. The WTE is a measure of the relay section's capability of transferring an exciton from the initial Cy3.5 to the AF647 without considering the efficiency of the initial Cy3.5 excitation. As a result, the WTE values are always higher than E_{ee}. The formula for WTE is presented in eq 3

$$\text{WTE} = \left(\frac{\Phi^{\lambda_B,T}_{AF647} - (f \times \Phi^{\lambda_G,T}_{AF647})}{QY^{T}_{AF647}} \Big/ \frac{I^{\lambda_B,T}_{Cy3.5}}{QY^{T}_{Cy3.5}} \right) \tag{3}$$

The parameters are similar to those in eq 1 with $I^{\lambda_B,T}_{Cy3.5}$ being the photon count emitted by the Cy3.5 dyes in the presence of AF488 dyes and absence of AF647 dyes when exciting with the blue light source.

The other basic characterization is MPW physical length. We report not the physical size of the DNA but the linear path covered by the energy transfer, defined as the distance between the AF488 and AF647 dyes. We note that the HomoFRET presents a random-walk movement, meaning that there will be a considerable number of "backward" steps along the MPW; we did not consider these when calculating the MPW length. Therefore, the full length of the photonic MPW with input-relay-output dyes was 29 nm long, which, as seen below, is shorter than the physical length of the DNA origami, which is 42 nm. We are aware that other variables such as buffer conditions, including the choice of Mg^{2+} concentration, may modify DNA nanostructure size, and as such, the dye positioning could vary, modifying the 29 nm reported length.[42,43] Although as it is the interhelix, and not the linear dsDNA length, that is more susceptible to these changes, we maintain that the effect in our case is minimal.[4]

Theory. A discussion of both FRET and the motivating hypothesis that greater dye density would increase transfer through the HomoFRET relay is warranted at this time. FRET occurs through the dipole−dipole coupling of an excited donor molecule to a ground-state acceptor molecule. As such, the equations that represent the efficiency of transfer (E_{FRET}) for a single donor−acceptor (D−A) pair are given as follows[44]

https://dx.doi.org/10.1021/acsanm.0c00038
ACS Appl. Nano Mater. 2020, 3, 3323−3336

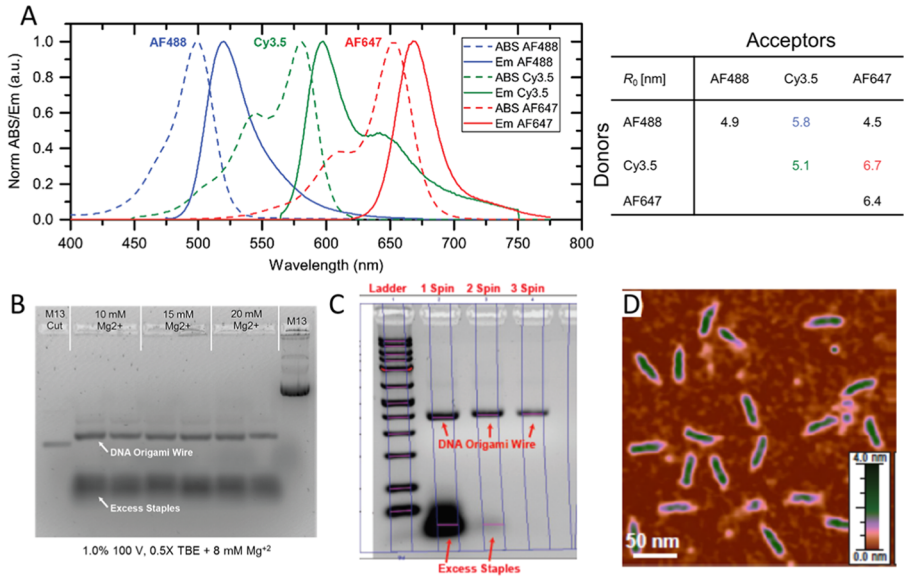

Figure 2. Characterization of origami MPW. (A) Normalized absorbance and fluorescence of dye components. Table with calculated Förster distances in nm. (B) 1% Agarose gel of DNA origami formed at varying Mg^{2+} concentrations. (C) 1% Agarose gel of DNA origami before and after Amicon 50 kD purification. (D) Atomic force microscopy (AFM) in dry mode of DNA origami after purification.

$$E_{\mathrm{FRET}} = \frac{(R_0/r_{\mathrm{DA}})^6}{1 + (R_0/r_{\mathrm{DA}})^6} \tag{4}$$

$$R_0{}^6 = C_0\kappa^2 J n^{-4}(\mathrm{QY_D}) \tag{5}$$

The r_{DA} is the D−A distance, and R_0 is the Förster distance, which is the separation distance between D and A where FRET will occur with 50% efficiency. The R_0 can be obtained from the physical parameters in eq 5; C_0 = 0.021 and κ^2 is the dipole orientation factor (typically assumed to be 2/3 for most randomly oriented ensemble systems, but best estimated as 0.4 for static DNA conjugated dyes),[45] $\mathrm{QY_D}$ is the quantum yield of the donor, n is the refractive index of the medium (1.33 in aqueous buffers), and J is the spectral overlap integral in units of $\mathrm{nm^4\ M^{-1}\ cm^{-1}}$.[26,44] As is clear in eq 4, the efficiency of FRET correlates with the D−A distance to the sixth power.

If we return to the FRET efficiency equation, we can rewrite it in terms of the decay mechanisms of the excited state.

$$E_{\mathrm{FRET}} = \frac{k_{\mathrm{T}}}{k_{\mathrm{F}} + k_{\mathrm{NR}} + k_{\mathrm{T}}} \tag{6}$$

where k_{F} and k_{NR} are the fluorescence and the nonradiative decay rate constants, respectively. k_{T} is the FRET transfer rate. Combining eqs 4 and 6 indicates that k_{T} is inversely proportional to $(r_{\mathrm{DA}})^6$ (assuming that dye proximity to each other does not modify the other parameters).

$$k_{\mathrm{T}} = \left(\frac{R_0}{r_{\mathrm{DA}}}\right)^6 \times (k_{\mathrm{F}} + k_{\mathrm{NR}}) \tag{7}$$

We must now consider the HomoFRET transfer,[46] taking into account the random-walk characteristics. The relay is best described as a one-dimensional symmetric random-walk with a mirror edge and a defined probability for absorption by the AF647.[47,48] The successful relay capability of the Cy3.5 HomoFRET section is therefore given by the probability of transfer to the AF647 by an exciton with ψ steps on an MPW with n step length, assuming that the exciton begins on the Cy3.5 farthest away from the AF647; this value is estimated by the distribution function[47]

$$P(\mu, \psi) = \frac{\int_1^{\psi} \frac{1}{\sigma\sqrt{2\pi}} e^{(-(\psi-\mu)^2/2\sigma^2)} d\psi}{\int_1^{\infty} \frac{1}{\sigma\sqrt{2\pi}} e^{(-(\psi-\mu)^2/2\sigma^2)} d\psi} \tag{8}$$

The ψ value is more accurately defined as the average number of steps available to each exciton and as such is an ensemble property that is not required to be an integer; ψ is determined by the fluorescent lifetime (τ) multiplied by the FRET transfer rate (k_{T}). The μ is the average number of steps required before reaching the absorbing edge or wire terminus, and σ is the variance of μ as estimated in eqs 9 and 10. The probability of absorption by the output, α, is comparable to E_{FRET} from Cy3.5 to AF647.

$$\mu = n\left[\alpha^{-1} + \frac{1}{2q}(n-1)\right] \tag{9}$$

$$\sigma^2 = \frac{n}{6q^2}\left\{n^3 + \frac{2q-a}{a}[2n^2 + 1 - 3q] + \frac{n}{a^2}[6q(q-a) + a^2(2-3q)]\right\} \tag{10}$$

In the symmetric random-walk, q represents the efficiency of HomoFRET between Cy3.5 pairs and is the variable being modified by changing the Cy3.5 dye density along with n. To utilize these analytical solutions, we must assume that the Cy3.5 relays are evenly spaced and are all equivalent (which assumes that there are no trap sites). Although this does not fully hold for all of the experimental MPWs, it is a good initial approximation for the full- and half-density MPWs (Figure 1). The average number of steps required by an exciton to traverse a HomoFRET relay increases to the second power as the number of physical steps increases. In other words, it requires more steps to cover the same distance as the dye density increases. This is the crux of the issue: increasing the dye density requires more transfer steps (μ correlating with $\sim n^2$), which would decrease

https://dx.doi.org/10.1021/acsanm.0c00038
ACS Appl. Nano Mater. 2020, 3, 3323−3336

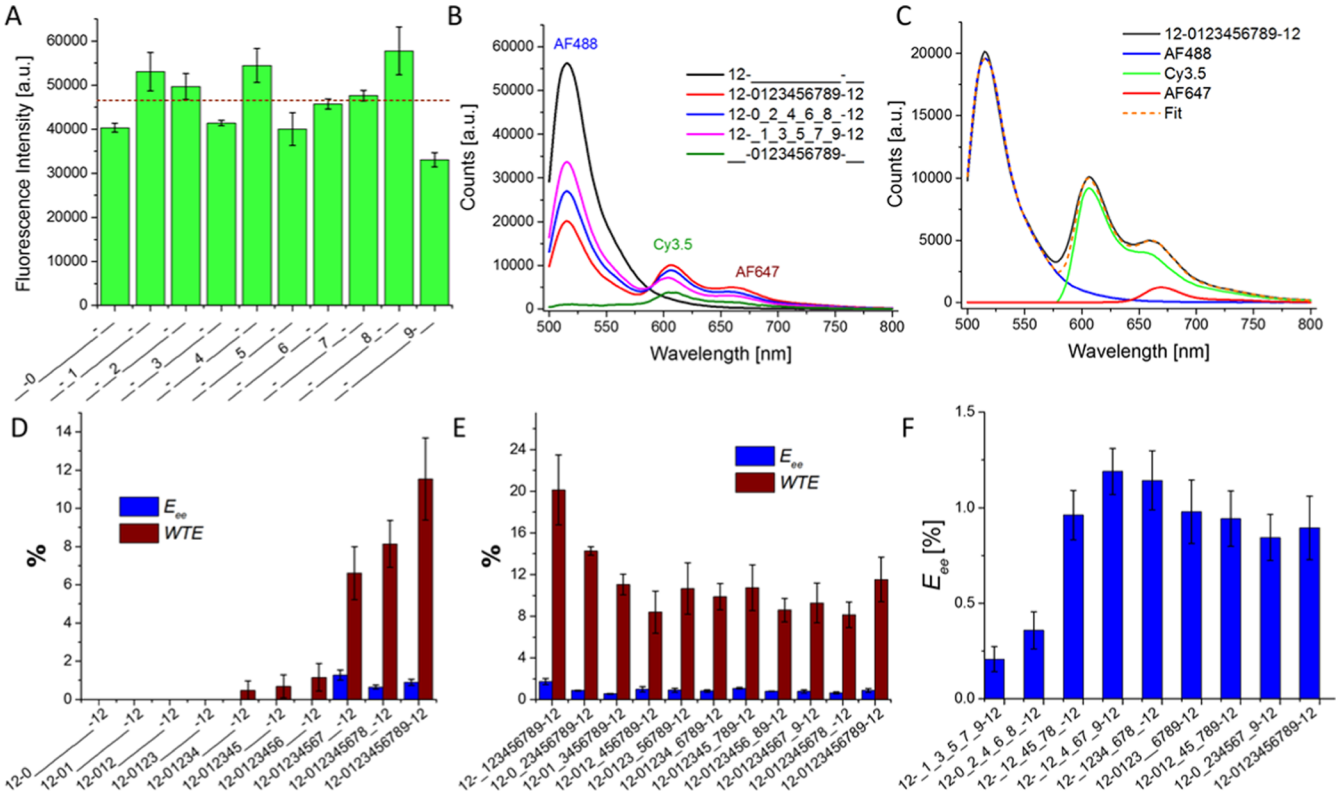

Figure 3. High-throughput steady-state fluorescence characterization of MPWs. (A) Fluorescence intensity of individual Cy3.5 positions excited at 585 nm. Corrected by absorbance. Dashed line is average intensity. (B) Fluorescence spectra of some representative MPWs. Excitation at 466 nm. (C) Spectral decomposition of 12-0123456789-12 MPW. (D) E_{ee} and WTE values of MPWs as the Cy3.5 HomoFRET relay section was built up. (E) E_{ee} and WTE values of MPWs missing a single Cy3.5. (F) E_{ee} values of MPWs with varying Cy3.5 densities (left to right, from the lowest to highest Cy3.5 density).

the MPW efficiency. Yet, the increased density should increase k_T by the sixth power, as r_{DA} is shorter for each step. At high FRET efficiencies, the increase in k_T should result in a faster growth of the average available steps, ψ, outpacing the negative effect of higher step requirements. This was supported by Monte Carlo simulations realized for previous HomoFRET bridges.[30]

MPW Structural Characterization. We constructed a 29 nm long linear photonic wire within a 42 nm long DNA nanostructure, with the 29 nm transfer distance being similar in length to the longest recorded DNA MPW.[30] The MPW can be broken down into a two-dye input/donor segment (AF488), a 10-mer HomoFRET relay segment (Cy3.5), and a two-dye output/acceptor segment (AF647). The input and output dyes were individually addressable, and we realized experiments where only a single AF488 or a single AF647 was included (see spFRET experiments for example). To determine the E_{ee} values, we found it optimal to only consider MPW with zero or two dyes in the input and/or output, *i.e.*, for both the AF488 and the AF647. Cy3.5 was chosen as the relay dye as previous works demonstrated its excellent HomoFRET capability, while also functioning as an acceptor to AF488 and donor to the final output.[29,30] A table is available in Figure 2 that shows the Förster distances of the dye pairs, including the Cy3.5−Cy3.5 Homotransfer, R_0 = 5.1 nm. We note that the choice of the three dyes was also purposeful to minimize absorption overlap and direct downstream photonic excitation. The fluorophores were arranged inside a 6-helix origami bundle formed from a truncated version of the M13mp18 plasmid;[49] details are available in the Materials and Methods section, and the full DNA list and preparation protocol are available in the Supporting Information (SI). All of the fluorophores were attached to the 5′ end of staple strands, with the attachment locations for the fluorophores carefully selected to ensure their preferential orientation toward the center of the six-helix bundle nanotube. The design was chosen to obtain close dye proximity at maximum density, with a separation of only ∼2.15 nm based on bp separation, allowing for very efficient predicted FRET and HomoFRET without transitioning to other coupling regimes.[37] As has been seen for cyanine and Atto dyes, separations below 2 nm lead to coupled dye systems, which tend to have diminished fluorescent properties.[37,38] To represent the individual wire configurations, the naming convention shown in Figure 1c was adopted. A number represents that the dye is present at the respective location, whereas an underscore, "_", indicates that the unlabeled strand has been used. Dashes, "-", signify the boundary between different fluorophore domains. For example, the full MPW, signifying maximum dye integration and highest relay density, is represented as 12-0123456789-12. The full MPW had twice the relay dye density of a wire missing alternate Cy3.5 dyes, represented as 12-_1_3_5_7_9-12, as shown in Figure 1c. An MPW with similar relay density but with different positional Cy3.5 would be 12-0_2_4_6_8_-12; these two structures represent the half-density MPWs. These structures will be often used in subsequent discussions, where they may be referred to as full- and half-density MPWs. As mentioned, there are 1024 permutations just within the HomoFRET relay, though many exhibit negligible transfer through the MPWs (*e.g.*, a completely empty set). Using the high-throughput capabilities of DNA nanostructures, we were able to test 147 different configurations with up to 15 repeats of individual MPWs.

https://dx.doi.org/10.1021/acsanm.0c00038
ACS Appl. Nano Mater. 2020, 3, 3323−3336

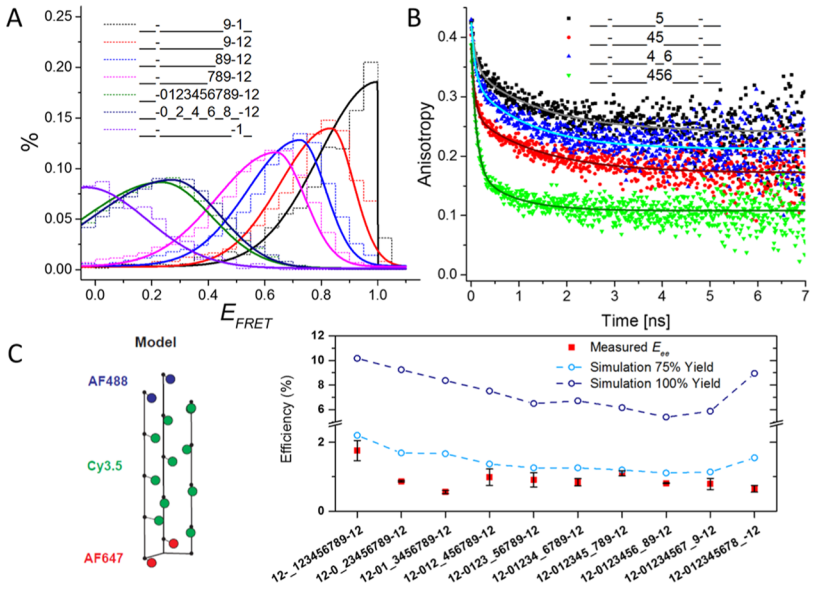

Figure 4. Additional MPW characterization. (A) spFRET of varying MPW structures. Fits are bi-Gaussian. (B) Fluorescence lifetime anisotropy of Cy3.5-only MPWs. Fits are double-exponential decays. (C) Schematic of the structure used in Monte Carlo simulations and predicted (dashed lines) and experimental E_{ee} values (red squares). The dark-blue line represents the simulated efficiencies assuming that the MPWs were 100% perfectly formed, and the light-blue line assumes that 75% of the dye-labeled DNA is correctly placed with 25% in solution. The 75% line is not a fit, merely a representation of the expected values if only 75% of the MPW were correctly formed.

A crucial component in DNA nanostructure design is confirming the formation yields;[50] the MPWs were evaluated by gel electrophoresis and atomic force microscopy (AFM).[43] A 1% agarose gel was used to determine the optimal formation and purification strategies; it was determined that the best-formed origami was obtained at 15 mM Mg^{2+}. Figure 2C demonstrates how 50 kD Amicon cutoff filters allowed for purification of the MPWs and elimination of excess staple strands to obtain purified MPWs at greater than 90%, a value supported by spFRET experiments (*vide infra*). We note that these characterizations do not discount slightly misformed MPWs that are indistinguishable on a physical level but have missing staple strands.[50] Super-resolution microscopy techniques are capable of distinguishing these deficiencies but are labor and equipment intensive.[50,51] The annealing process (see Table S3 in the SI) was chosen to minimize this possibility. AFM scans of the formed origami wire (Methodology and additional Figure S1 available in the SI), post Amicon purification, are also seen in Figure 2D. It was observed that most wires were generally well-formed. The measured wire dimensions from the AFM (l = 42 ± 1.5 nm and w = 10.5 ± 1.2 nm, 61 wires measured) were in agreement with the wires' design dimensions. Utilizing a dried sample deposited on mica resulted in the collapse of the 6-helix bundle; we therefore do not believe that the height measurement is representative of the DNA structure diameter in solution.

Solution-Based Fluorescence Characterization. We began the spectral analysis by characterizing the MPWs, ensuring that each individual Cy3.5 site was addressable (Figure 3A) and that the fluorescence intensity increased with increasing Cy3.5 (Figure S2). The fluorescence intensities in Figure 3A were normalized to the 260 nm absorbance to ensure that differences in concentration did not account for the variability. As seen in Figure 3A, the variability in the Cy3.5 positions was larger than expected with an intensity deviation of 15% over the varying sites. Experimental E_{ee} values of the extensive MPW design space are obtained using the steady-state fluorescence spectra of the MPW (Figure 3B,C). For example, the systems in which we built up the MPW in a sequential manner (Figure 3D), MPWs with a single Cy3.5 missing (Figure 3E), and a multiplicity of MPWs with varying Cy3.5 densities (Figure 3F) are shown. The chosen structures were based on intuitive guesses of which of the 1024 variations would provide the most informative results. In this manner, we investigated ∼10% of the HomoFRET relay design space with over 500 individual measurements. The experimental E_{ee} values only reached 0.5−1.5%, with the WTE values also limited to the ∼8−20% range. As can be seen in Figure 3F, the full-density MPW (far right, E_{ee} = 0.90 ± 0.15%) does have a statistically significant greater transfer efficiency than the half-density MPWs (far left, 12-_1_3_5_7_9-12 and 12-0_2_4_6_8_-12: E_{ee} were 0.21 ± 0.07% and 0.36 ± 0.10%, respectively), yet adding a single Cy3.5 to create 12-_12_45_78_-12 (third from left, E_{ee} = 0.96 ± 0.13%) results in an equivalent E_{ee} as the full MPW.

The high-throughput fluorescence measurements resulted in low E_{ee} MPWs independent of the relay design; further in-depth spectral characterization was required to determine structural or design flaws affecting the MPW's efficiency. This included steady-state determinations of individual FRET efficiencies of the AF488 to Cy3.5 and Cy3.5 to AF647 steps (Figure S3). We utilize the bracketed notation {Cy3.5 position} when discussing a specific position in the HomoFRET relay section. The E_{FRET} from AF488 to Cy3.5 increased as additional Cy3.5 were added but saturated once Cy3.5 positions {0, 1, and 2} were included, going from 0.50 ± 0.04 to 0.60 ± 0.05 and stabilizing at 0.65 ± 0.02 (Figure S4). As the α parameter (from eqs 9 and 10) is crucial to both the E_{ee} and WTE values and can be estimated as the E_{FRET} of the Cy3.5 to AF647, we utilized multiple quantization strategies. This included steady-state fluorescence, lifetime fluorescence, and spFRET to determine the most representative value.[52] See Figures 4 and S4 for the spectra. The steady-state and time-correlated single-photon counting (TCSPC) spectroscopy reported values of α = 0.55 ± 0.06%. The spFRET results demonstrated that the MPWs were not

https://dx.doi.org/10.1021/acsanm.0c00038
ACS Appl. Nano Mater. 2020, 3, 3323−3336

Table 1. Predicted Values of E_{ee} of the Full- and Half-Density MPWs Based on FRET Efficiency Using the Ideal Predicted Values (Theory) or the Experimentally Determined Values (Experiment)[a]

MPW		$E_{FRET}^{AF488-Cy3.5}$	α	q	k_T [ns^{-1}]	ψ	μ	σ	E_{ee} [%]
full	theory	0.997	0.999	0.994	90.0	188.9	45.2	33.0	99.9
	experiment	0.65 ± 0.02	0.83 ± 0.09	0.7 ± 0.1	1.3	2.7	60.0	45.6	0.9
half	theory	0.935	0.970	0.762	1.6	3.4	11.8	8.1	9.8
	experiment	0.50 ± 0.04	0.8 ± 0.1	0.6 ± 0.2	0.7	1.5	15.2	10.7	1.0

[a]Values with uncertainties are experimentally determined values. All other values arise from estimated dye positions and the analytical model.

composed of bimodal distributions with high-efficiency and low-efficiency MPWs but instead had a broad distribution of efficiencies as generally seen in DNA−dye systems.[53,54] The spFRET values for α went from 0.64 ± 0.15 for __-_____789-12 up to 0.84 ± 0.13 for __-_____9-12 (seen in Figure 4A). These initial results eliminated bimodal (high E_{ee}/low E_{ee}) MPWs due to missing DNA strands, which some reports predict to be around 9% for DNA origami structures,[51] which would presumably disrupt FRET. Nor would origami formation efficiency justify the lower transport efficiency. Both the input and output steps of exciton transfer were considerably lower in efficiency than predicted based on bp separation, yet they follow expected FRET tendencies.

To obtain greater insights into the Cy3.5 dye and how it acted as a bridge/relay, we performed TCSPC spectroscopy and fluorescence lifetime anisotropy. Similar to what was observed when the individual Cy3.5 locations were interrogated in the steady state (Figure 3A), it was observed in the TCSPC data that the position of the Cy3.5 altered the fluorescence lifetime (τ, we note that τ represents the amplitude average lifetime of the measurement)[55] ranging from 1.8 to 2.5 ns (see Table S4 and Figure S4 in the SI),[56] providing further evidence that the HomoFRET relay could not be considered entirely homogenous. As an example, we determined the τ of the interior Cy3.5 positions, specifically {4, 5, and 6}, when measured as a lone Cy3.5 dye $\tau_{\{5\}}$ = 2.14 ± 0.13 ns, the addition of position {4} results in a drop off $\tau_{\{4,5\}}$ = 1.81 ± 0.18 ns, and then with position {6} measured as $\tau_{\{4,5,6\}}$ = 2.16 ± 0.14 ns. We then eliminated position 5 and obtained the highest $\tau_{\{4,6\}}$ = 2.48 ± 0.13 ns. Clearly, the τ is position dependent, and it has been previously shown to be attachment and DNA nucleotide sensitive (*e.g.*, whether attached to A-T or C-G bps),[57−59] but in this case, the τ appears to be modified by labeling of the neighbor positions.

Fluorescence lifetime anisotropy was further used to determine the estimated efficiency of HomoFRET. The fluorescence lifetime anisotropy values directly report the experimental $E_{FRET}^{Cy3.5-Cy3.5}$, q, for the two MPWs, and with τ, we can get k_T and ψ (see eqs 8−10). We utilized 2.1 ns as a representative average of all Cy3.5 localized excitons τ although the above measurements show that the assumption is not fully valid, we find that it is an adequate first approximation. In Figure 4b, we present the lifetime anisotropy curves for a single Cy3.5, position {5}, with an average decay time of 1.08 ± 0.09 ns. This indicates that the Cy3.5 adopts configurations where it has good rotational mobility within the 6-helix bundle. The data also present an extended residual anisotropy (0.24 ± 0.01), which suggests that the Cy3.5s can also interact with the DNA and exhibit a relatively slow fluorescence depolarization as expected of a dye complexed with a large structure. The measurements are of an ensemble average nature, and the Cy3.5 is known to have dynamic interactions with the DNA scaffold.[60] Yet, these interactions can appear static on the time scale of the fluorescent lifetime measurement. We measured the nearest neighbor {4,5}, a skip neighbor {4,6}, and two nearest neighbor {4,5,6} situations to obtain the HomoFRET estimates for the full MPW and the half-density MPW. We observed decreases in both the average anisotropy decay time as well as the residual anisotropy (see Table S5 for fits) as would be expected for samples undergoing HomoFRET; from these experiments, we could determine the q values required for the analytical model (see the next section).

Ideal Efficiency Estimation and Computational Models. We will briefly focus on the predicted E_{ee} values of the full- and half-density MPWs based on the previously discussed theory. Initially, we assumed DNA design-based dye positions, from which arise the dye distances and E_{FRET} values. The analytical random-walk model was applied to the theoretical MPWs, and we can rewrite E_{ee} as a function of the individual step efficiencies

$$E_{ee} = E_{FRET}^{AF488-Cy3.5} \times P(\mu, \psi) \times \alpha \quad (11)$$

Assuming 2.15 nm separation for all dyes (D−A distances are based on the length of dsDNA per bp extension), as was the aim for the full-density MPW (12-0123456789-12), and using the R_0 values in Figure 2, we obtain a predicted E_{ee} value of 99% for the full-density MPW. Similarly, using the 4.2 nm predicted separation in the HomoFRET relay section in the half-density MPWs, we get an E_{ee} value of 9.8%. As noted in the previous section, we utilized the fluorescence characterization strategies to determine experimental estimates of the transfer efficiencies of each step. We compare the predicted values to the experimentally obtained values and then propagate the values into predicted E_{ee}; all of these values are available in Table 1.

We also realized detailed Monte Carlo simulations to predict ideal efficiencies. The model has been previously described in the literature,[24,29] while the basic assumptions are presented below. The simulations assumed that the fluorophores interacted solely via point dipole−dipole coupling. The DNA was modeled as three parallel straight arms with dyes positioned on the theoretical design positions and directed perpendicular to the DNA and with the azimuthal angle directed into the center with dye linker lengths assumed to be 0.75 nm. The dyes were allowed to move randomly and swing freely at their attachment points but had static dipoles for the FRET (random static orientations and distances), so that κ^2 depended on the specific D−A orientation. This consideration is important as the random-walk model assumes a fixed DNA-based dye position (*i.e.*, κ^2 = 0.4, and fixed distances). The Monte Carlo simulations returned more restrained E_{ee} values with the 12-0123456789-12 MPW topping out at E_{ee} = 15.1%. The lower E_{ee} results from the high probability of unfavorable dye orientations,[61,62] which is a more significant effect than the range of efficiencies resulting from inhomogeneity in the dye position.[63] The Monte Carlo simulation results for the series of MPWs with an individual Cy3.5 missing are shown in Figure 4C. The ideal device curve is depicted as a dashed line and assuming that all of the dyes are

https://dx.doi.org/10.1021/acsanm.0c00038
ACS Appl. Nano Mater. 2020, 3, 3323−3336

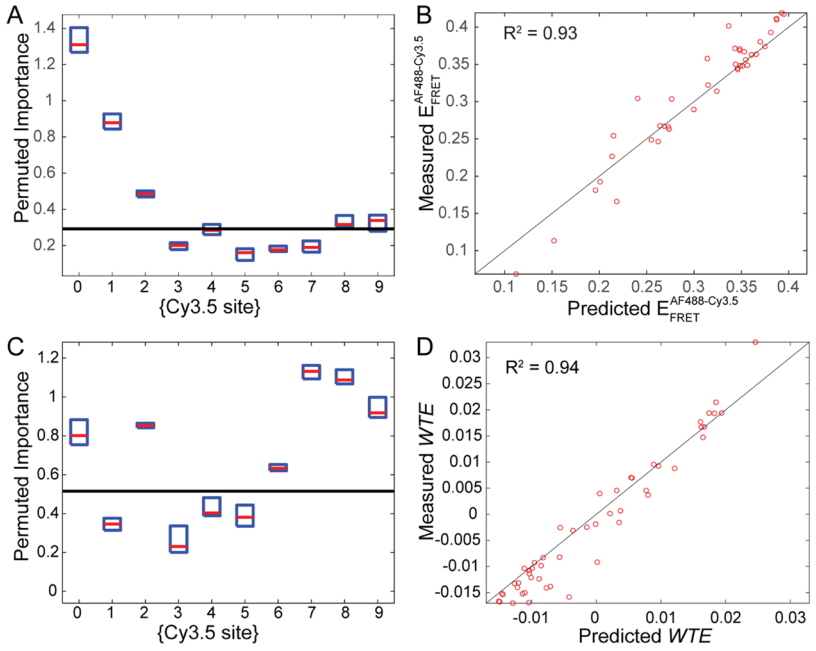

Figure 5. Random forest regression results. The box plots indicate the median and the first and third quartile values. The horizontal black line is the null result. (A) Permuted importance of the Cy3.5 site to the $E_{FRET}^{AF488-Cy3.5}$. (B) Predicted vs experimental results of the $E_{FRET}^{AF488-Cy3.5}$. (C) Permuted importance of the Cy3.5 site to WTE. (D) Predicted vs experimental results of WTE.

attached to the DNA template, the simulation predicted values range from 10.2 to 5.4% E_{ee}. The experimental and estimated E_{ee} differed considerably in value though following a similar trend. The Monte Carlo simulations predicted that removing the end Cy3.5 positions {0 and 9} of the HomoFRET relay would reduce the E_{ee} the least.

Using random forest machine-learning regression algorithms, a quantitative model was developed capable of predicting the figures of merit, E_{ee} and WTE, based on the chromophore attachment configuration (Figure 5B,D). Conversely, the model can infer the importance of particular input variables such as the attachment status of each chromophore to a value such as $E_{FRET}^{AF488-Cy3.5}$ or WTE; see Figure 5A and C, respectively. For the random forest model, the importance indicator is a description of how each degree of freedom affects the quality of the predictive output. In principle, an importance metric might be constructed by removing each degree of freedom from consideration, in turn, and observing how much predictions deviate from the known data compared to the full model. However, removing a degree of freedom entirely changes the statistics, making it a poor proxy of the original model. To address this issue, the permuted importance was devised.[64] It breaks the relationship between each degree of freedom and the output while retaining the statistics. It does so by randomly reassigning the values within the degree of freedom. Here, we repeat this randomization 10 times, to generate the box plots shown in Figure 5. These box plots indicate the median, as well as the first and third quartiles.

We found that the WTE values provided a more robust data set for analysis, as there was more variation, which made it more suitable for the algorithm. As would be expected, the WTE is mainly affected by the Cy3.5s near both the donor and the acceptor, though some interesting dependencies emerge (Figure 5C). For instance, the Cy3.5 site {1} is less influential than would be expected based on a comparison to site {8} on the acceptor side. However, observing the AF488 component of the steady-state fluorescence spectra and applying the machine-learning regression confirm that site {1} is important as a quencher of the AF488 (Figure 5A). Therefore, the random forest results suggest that site {1} is able to extract energy but then does not meaningfully contribute to its further transport, signifying that this site may act as a trap. These two findings are consistent with the energy transfer efficiency ultimately being more bottlenecked by random-walk processes through the Cy3.5 relay, rather than the rate of energy transfer from AF488 to Cy3.5.

Characterization of MPW Film Samples. As we have shown in a previous work, DNA MPWs demonstrate increased efficiency when cast in thin films and also with cryogenic cooling; the respective improvement is more notable the greater the number of dyes in the MPW as the systems' efficiency improves due to increased FRET efficiency of each individual step.[34] The DNA origami-based MPWs were ideal candidates for this methodology due to their extended length and large HomoFRET relay section. Through what we previously learned in the solution-based characterization, we tested a series of MPWs that indicated that they might have the highest efficiencies. Poly(vinyl alcohol) (PVA, M_w 31 000−50 000. Sigma-Aldrich) films, 50 nm thick, with homogenously dispersed MPWs were prepared for characterization on a plasma-cleaned SiO_2/Si substrate.[65]

We raster-scanned the laser over a 50 × 50 μm^2 area in 5 μm steps creating a hypermap, summing over the entire map to get the final spectra. As can be seen in Figure 6A, the PVA film is quite homogenous in MPW distribution. A 532 nm cutoff filter is built into the system to avoid the laser scattering signal; unfortunately, this resulted in that part of the AF488 signal being cut off (see Figure 6A,B). This partial AF488 peak was still sufficient for spectral fitting/deconstruction and to determine the initial photon count, under the assumptions that the AF488 does not have a large Huang−Rhys factor in this medium[66] and

https://dx.doi.org/10.1021/acsanm.0c00038
ACS Appl. Nano Mater. 2020, 3, 3323−3336

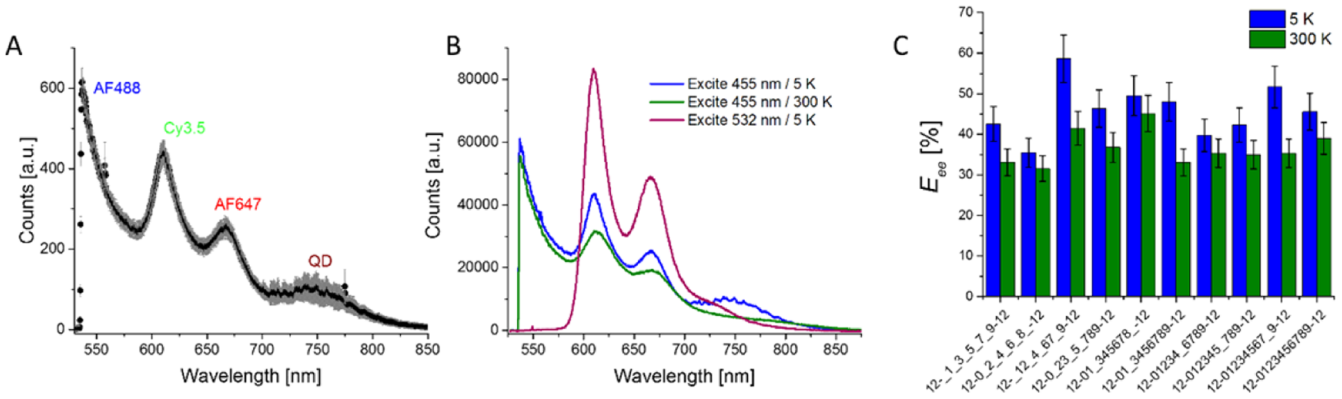

Figure 6. Fluorescence spectra of MPWs dispersed in PVA films. (A) Average (black dots) and standard deviation (gray) of an individual fluorescence spectra of the full-density MPW at 5 K. Excited at 455 nm. The individual component peaks are labeled, including the internal standard QD (see Materials and Methods). (B) Summed fluorescence spectra of full-density MPW at 5 or 300 K and excited with 455 or 532 nm. (C) E_{ee} values at 5 K (blue) and 300 K (green).

can be adequately represented by its solution-based spectra—assumptions that held for the Cy3.5 and AF647.

Quantification of E_{ee} was done in the same manner as in the solution measurements using eq 1 and a 532 nm laser (λ_G) to correct for downstream excitation by the 455 nm laser (λ_B). Control samples containing no AF488 all resulted in E_{ee} values of approximately 0, validating the approach. Additional measurements available in the SI (Figures S5 and S6) include the individual component controls, *i.e.*, AF488, Cy3.5, and AF647 utilized for spectral deconstruction, as well as baseline intensities, and calculation of the f correction factor for eq 2 and $\Phi_{AF488}^{\lambda_B,T}$. The fluorescence QY in the PVA film at lower temperatures increased for all three dyes (see Table 2 for all QY data). In general, positioning dyes in films increases fluorescence due to changes in environmental polarity, increased rigidity, and inhibition of dimer formation,[67] though in this case the QYs at RT were actually higher for the solution measurements. It is possible that the nanotube of the 6-helix bundle favored dye rigidity in a similar manner as PVA films generally do. It is also possible that quenching effects due to the PVA itself decreased the dye QYs. We observed a similar result in our previous DNA–dye MPWs analyzed in PVA films.[34] By lowering the T, a suppression of vibrations and the corresponding phonon-mediated nonradiative relaxation pathways, as well as cis-trans isomerizations of the cyanine dyes, is achieved. This resulted in higher QYs at lower T.[16,68]

Table 2. Fluorescence Quantum Yields of Dyes in Different Environments[a]

condition	AF488	Cy3.5	AF647
solution	0.95	0.59	0.52
PVA film 300 K	0.69	0.30	0.46
PVA film 5 K	0.96	0.39	0.53

[a]The solution QYs were calculated using known standards fluorescein, Rhodamine640, and Rhodamine800. The PVA films' QYs were determined using a QD standard as detailed in our previous publication.[34] All QY values have uncertainties in the range of 0.07.

The end result was that the E_{ee} increased drastically within the PVA film, going from ~1% in solution to ~40% in the films, with a further increase to ~50% at 5 K. The increase was considerable for all of the chosen samples. The highest efficiency MPW was 12-_12_4_67_9-12 at E_{ee} = 59 ± 6%. This design was an improvement over the half-density MPWs (<43%), but similar to what was seen in Figure 3F, multiple intermediate-density MPWs were within the experimental uncertainty of having analogous efficiency. The full-density MPW was slightly lower with E_{ee} = 46 ± 5% at 5 K.

DISCUSSION

The origami design for the MPW surpassed previous DNA templated MPWs, generally based on simple dsDNA or tile systems, by allowing greater dye density and individual site addressability. Analytical and simulation models predicted high-efficiency transfer in the high-density MPWs, in large part motivating the investigation. An extensive data set using high-throughput steady-state fluorescence showed that the results differed significantly from the predicted values independent of what Cy3.5 relay design was used. In solution, the E_{ee} values remained in the 1% range as determined by ensemble steady-state fluorescence spectroscopy. This low efficiency was initially assigned to misformed structures, decreased input and output FRET efficiencies, and/or decreased efficiency of the Homo-FRET relay section.

Structural characterization including agarose gels and AFM showed that the samples were greater than 90% well-formed DNA origami structures. Even with well-formed origami, it is possible that missing dye strands could result in truncated efficiency species.[24] The Monte Carlo simulations suggested this as a probable cause for the decreased E_{ee} values. The spFRET data showed that this was not the likely culprit as the distribution of FRET efficiencies was shown to be broad around the average FRET value. If misformed structures were the cause, we would have expected to observe bimodal distributions.[53] Similarly, the higher E_{ee} values reported in PVA films dispel formation efficiency as the root cause, since the defects would have transferred to the films as well.

The decreased input–output FRET efficiency, seen in Table 1, clearly plays a role in the decreased photonic transfer in solution. Yet, when considering the relative effect on the E_{ee} values, they merely limit the upper bound of efficiency from 99% down to 55%. Considering that these are merely two FRET steps in a system that is numerically dominated by the HomoFRET relay, it is not surprising that the decreased transfer efficiency in the relay section is the principal cause of inefficiency. It may appear that the decrease is not that large, the q value going down from 0.99 to 0.73, but if we consider that in the full-density

https://dx.doi.org/10.1021/acsanm.0c00038
ACS Appl. Nano Mater. 2020, 3, 3323–3336

MPW an average of 45 HomoFRET steps (see μ in Table 1) will be required to get to the AF647, this small decrease adds up quickly. In fact, once we have the experimental FRET values, the analytical model predicts E_{ee} that correlate remarkably well with the measured values for the MPW. We anticipated 0.9% E_{ee} ($\pm$0.3%) and measured 0.90 $\pm$ 0.15% E_{ee} for the full MPW. For the half MPW, 1.0% E_{ee} ($\pm$0.4%) was expected, while the experimental values for 12-0_2_4_6_8_-12 and 12-_1_3_5_7_9-12 were 0.36 $\pm$ 0.10% and 0.21 $\pm$ 0.07%, respectively. Evidence supporting this result was also provided by the machine-learning methodology as it was found that the Cy3.5 site {1} was overall harmful to transfer even as it was positive for maximizing the input efficiency. Although surely all three components play a role, it is apparent that the individual Cy3.5−Cy3.5 HomoFRET efficiencies are the greatest limitation in the MPW transfer capability. One explanation is the possibility of forming short-lived dye dimers, exciplexes, with neighboring positions, which tend to have increased nonradiative decay rates.[39,69] Large discrepancies between the predicted FRET rate and the measured FRET rate, ~10 times slower, for closely packed cyanine dyes (<2 nm) on DNA have also been observed in the past.[37] It appears that FRET's point-dipole approximation is not fully valid at these short separations, which are similar to the length of the cyanine dyes.[44]

The solution-based systems appear to have inherent transfer limitations independent of the relay dye density, yet in the case of MPW in PVA films, the efficiencies are greatly enhanced. This increase is outstanding considering that the previously reported highest E_{ee} for a DNA MPW was 6% at a length of 24 nm; not only are these MPWs longer by 21% but also an order of magnitude more efficient.[34] In films, FRET approaches the DNA design predicted efficiencies for HomoFRET as well as the input and output steps, and as such, the MPWs' transfer efficiencies are closer to the ideal values. We also note that this is not an artifact of dye QYs, a parameter that E_{ee} is very susceptible to, as the QY ratio in PVA 5 K is almost identical to the solution ratio. Nor is this due to inter-MPW interactions. We have calculated that 35 mM initial concentration would be needed for inter-MPW interactions,[34] while we are well below those concentrations at 10 nM. Control experiments have also shown that the MPWs are not interacting in the PVA film.[34] As of present, single wire imaging within the PVA film has not been feasible with our setup. We hypothesize that the marked improvement in transfer efficiency is due to reduced parasitic decay mechanisms of the individual dyes, reduced solvent interaction, along with increased rigidity, as well as reduced transitory dimers, all leading to increased FRET efficiencies. We recognize that this does not seem to be reflected in the calculated QYs, which suggests that the improvement is due to "improved" dye positioning, perhaps due to reduced flexibility or breathing of the overall 6-helix bundle. Additionally, there exists a possibility that the origami is "collapsing" within the PVA film (as seen in the AFM samples), and that in this manner with a reduced diameter, the dyes are brought slightly closer together, resulting in increased FRET. Changes in Mg^{2+} concentration can also modify the diameter of the 6-helix bundle, as higher Mg^{2+} values reduce interhelix distances.[42] In our case, the Mg^{2+} is reduced in the PVA films (~5 mM), as compared to the solution (15 mM), so it is unlikely to account for the increased transfer efficiency.

We return to our hypothesis on increased dye density resulting in increased E_{ee}; the solution-based measurements and the PVA film data provide some evidence, as the full-density MPWs are of greater efficiency than the half-density MPWs. Yet, the difference between the two confirmations is only slight, though statistically significant, at room temperature in both the solution and the film. Furthermore, MPWs with 6, 7, or 8 Cy3.5 all had greater E_{ee} values than the full-density MPW. The strongest support for the theory may arise from comparing the 6-helix bundle origami MPWs in this work to previous tile DNA MPWs; with similar HomoFRET extensions (~20 nm), the origami structure had up to 66% greater dye density and resulted in 10-fold increase in efficiency.[34] The extended theory we now postulate is that increased dye density does have an advantage (at higher E_{FRET} regimes), but that each additional step also adds an increased possibility of defects and trap states that curbs the improvement, and therefore a plateau of efficiency may be reached if these cannot be avoided.

CONCLUSIONS

In this work, we have developed a new MPW based on a DNA origami nanostructure. Our studies determined that in solution, cumulative losses limited the transfer efficiency of the MPW. We undertook extensive characterization and determined that diminished FRET efficiency of each individual step is the principal cause of the limited E_{ee} values. Using what we learned in the characterization as well as a solid-PVA film environment, an optimal-efficiency MPW was formulated and we can report transfer over 29 nm with 59% efficiency, which is 5 nm longer and 10-fold better than the prime DNA MPW previously reported.[34] The project began as a study of dye density on transfer in HomoFRET regions, the experiments providing some support that greater dye density results in optimized transfer. Yet, it appears that the FRET increase is often less than predicted due to imprecise dye localization and the creation of trap states; as such, optimization of DNA-scaffolded exciton networks will continue to require experimental as well as theoretical optimization. One important consideration continues to be the molecular context of the dye, meaning the neighboring bps, dye rigidity within the DNA nanostructure, and proximity of dyes for example. Some software tools take a few of these factors into account, and molecular dynamics can be helpful,[70,71] but these strategies are not currently part of the design process in most DNA photonic nanostructures. Nevertheless, the considerable improvement in the DNA-based MPW efficiencies reported here brings closer the promise of incorporation into new photonic technologies such as next-generation optoelectronic systems.

MATERIALS AND METHODS

Sample Preparation. Labeled and unlabeled DNA strands were obtained from Integrated DNA Technologies (Coralville) and Eurofins Operon (Huntsville). The sequences of the DNA can be found in Tables S1 and S2. All dye labeling was on terminal bases; succinimidyl ester labeling with a six-carbon linker was used for AF488 and AF647, whereas three-carbon linker phosphoramidite labeling was used for Cy3.5. Dye-labeled DNA strands are high-performance liquid chromatography (HPLC)-purified by the vendor; they are therefore assumed to have 100% labeling efficiency. For the 6-helix bundle DNA origami, a 704 nucleotide plasmid was prepared by cleaving the commercially available m13mp18 plasmid.[49] The DNA origami was prepared at 10 nM in 1× TAE (Tris base, acetic acid, EDTA) buffer with 15 mM Mg^{2+} with a 10-fold excess staple strand ratio. The annealing and purification strategy is detailed in the SI.

For the microscopy and cryogenic determinations, samples were spin-coated on plasma-cleaned SiO_2/Si substrates with a 90 nm oxide thickness (University Wafer, Boston) at a final MPW concentration of

https://dx.doi.org/10.1021/acsanm.0c00038
ACS Appl. Nano Mater. 2020, 3, 3323−3336

~10 nM in the original buffer with a 1% w/v poly(vinyl alcohol) (PVA, M_w 31 000−50 000. Sigma-Aldrich) addition. Spin-coating was performed by adding 22 μL of the solution to the SiO_2/Si substrate and then spinning the sample for 10 s at 1000 rpm (500 rpm/s ramp) followed by 30 s at 3000 rpm (1000 rpm/s ramp), resulting in an approximately 50 nm thin film with homogenous MPW distribution. Addition of a polymer-coated[72] 800 nm emitting QD internal standard (0.35 nM) was used to correct for any concentration effects.[34]

Spectroscopies. Additional spectra not included in the main text along with the corresponding fits are available in the SI.

Steady-state fluorescence was obtained by measuring 50 μL of the sample on a TECAN plate reader in 96-well plates using 466, λ_B, and 585 nm, λ_G, excitation wavelengths.

Absorbance spectra were taken on an Agilent 8453 UV−visible Chemstation with 1 cm pathlength and demonstrated that most samples were near the 10 nM concentration; when required, the absorbance spectra could be used to correct the fluorescence intensity.

For fluorescence lifetime determinations, a time-correlated single-photon counting technique using a Becker-Hickl SPC-630 board was used. The excitation laser was an 80 MHz 7 ps pulsed 532 nm frequency doubled diode-pumped Nd:YVO class 4 laser (High-Q picoTRAIN). The lifetimes were extracted by fitting a biexponential decay function to the collected fluorescence decays. An amplitude-weighted average was taken as the overall decay rate. In the same setup, polarizers were adjusted to the pertinent parallel and perpendicular settings to obtain the anisotropy measurements. The anisotropy decays were then fit with a dual exponential decay function.[37,73]

For the spFRET measurements, prior to adding the sample, the sample wells were soaked in a Tris-acetate-EDTA buffer solution with 15 mM Mg^{2+} and 1 mM bovine serum albumin for 30 min. Samples were prepared at 100 pM concentration, in a buffer solution containing 15 mM Mg^{2+} and 1 mM Trolox. The measurements were performed using 515 nm CW argon ion laser excitation. The light was directed into an Axiovert inverted microscope (Zeiss), where samples were illuminated through a 100× oil-immersion objective (1.4 numerical aperture, Zeiss). Their fluorescence was collected through the same objective. The in-focus portion of the fluorescence was retained by focusing through a 75 μm pinhole and then detected in two channels using a pair of single-photon avalanche detectors (Excelitas). The light at these two channels was distinguished by a dichroic mirror with a 640 nm cutoff (Semrock). For each sample, data acquisition was performed continuously for 20 min at a data acquisition rate of 1 kHz.[52]

Data analysis for spFRET was performed according to the following method, based on an approach by Pons et al.[74] First, the time-alignment was checked for the time series generated by the two data channels, by inspecting the coincidence of peaks. Then, data were retained if they contained at least 30 counts in a single channel or at least 40 counts in sum. The misattribution of the acceptor's fluorescence to the donor due to the portion of its signal below the cutoff frequency of 640 nm was determined by performing a FRET calculation using a sample containing only the acceptor chromophore (MPW: __-_____-1_).

A confocal microscope setup integrated with a close-cycle cryostat (Montana Instruments Corporation, Bozeman) allowed for the interrogation of the MPWs within PVA films at 5 and 300 K. The excitation sources were 455 nm (λ_B) and 532 nm (λ_G) lasers focused through a 0.42 NA long working distance objective with a 50× magnification. The laser spot diameter was determined to be ~2.4 μm, and the laser power was fixed at 20 μW for both lasers. The emission signal was directed to a 500 mm focal length spectrometer with a liquid nitrogen-cooled CCD (Princeton Instruments, Trenton). We note that due to the relatively large spot size, we are confident that the measurements are of ensemble quality and that we were not reading out individual MPWs.

Computation. Details of the Monte Carlo simulations are available in previous publications.[24,29] The physical structure has been discussed in the text; some additional premises are provided below. The approach used rate equations to describe the evolution of the dye excitations and an assumption that the dyes only interacted through the FRET mechanism. Since we treated target structures as incompletely formed and accompanied by assorted partial constructs/free dyes, we normalized the governing rate equations by the total concentration and the variables then become equivalent to probabilities. "Missing" dyes or free dyes were assumed to remain in solution and maintained a finite excitation probability.

For machine learning, a random forest method was selected to search the large configuration space while resisting overtraining.[64] We used 1000 decision trees, which were substantially higher than the threshold for the Monte Carlo error.[75] The hyperparameters, including the minimum leaf size and the number of predictors (bounded by the square root of the total population N), were optimized using Bayesian optimization to minimize the root-mean-square error of the model's correspondence to the test data.[76] These procedures were performed using Matlab's TreeBagger and Bayesopt algorithms.

The importance predictors were permuted to improve their baseline. This permutation process was independently performed 10 times to obtain statistics on how the randomized permutation affects the outcome.

The data set was unbalanced, typically with only a few individual data points bearing extremely high figures of merit, while the vast majority clustered toward an average score. During the bootstrap aggregation process, the data were mildly rebalanced by cutting the figure of merit's range into two equally wide bins and selecting an equal number of samples out of each bin during the random selection process. This process resulted in a higher chance of selecting from sparsely populated regions of the distribution, but the choice of using only two bins minimized the influence of the rebalancing procedure on the results. To account for this influence, an additional variable with randomized Boolean values was introduced as an uncorrelated variable. The importance of this variable was used to benchmark the threshold of meaningful significance. Any importance score lower than this uncorrelated variable is considered negligible. This "baseline" variable usually yields an importance score very close to 0 after permutation; however, rebalancing can cause it to rise.

■ ASSOCIATED CONTENT

Supporting Information

The Supporting Information is available free of charge at https://pubs.acs.org/doi/10.1021/acsanm.0c00038.

DNA sequence tables, purification protocols for cut M13 and DNA origami, AFM figures, fluorescence intensity data, steady-state FRET determinations, TCSPC fluorescence lifetimes and fits, fluorescence lifetime anisotropy fits, additional spectra of the MPW in PVA films, absorbance spectra, steady-state fluorescence spectra (PDF)

■ AUTHOR INFORMATION

Corresponding Authors

Igor L. Medintz − *Center for Bio/Molecular Science and Engineering, Code 6900, U.S. Naval Research Laboratory, Washington, District of Columbia 20375, United States;* orcid.org/0000-0002-8902-4687; Email: igor.medintz@nrl.navy.mil

Sebastián A. Díaz − *Center for Bio/Molecular Science and Engineering, Code 6900, U.S. Naval Research Laboratory, Washington, District of Columbia 20375, United States;* orcid.org/0000-0002-5568-0512; Email: sebastian.diaz@nrl.navy.mil

Authors

William P. Klein − *Center for Bio/Molecular Science and Engineering, Code 6900, U.S. Naval Research Laboratory, Washington, District of Columbia 20375, United States*

https://dx.doi.org/10.1021/acsanm.0c00038
ACS Appl. Nano Mater. 2020, 3, 3323−3336

Brian S. Rolczynski − *Electronic Science and Technology Division, Code 6800, U.S. Naval Research Laboratory, Washington, District of Columbia 20375, United States*
Sean M. Oliver − *Department of Physics and Astronomy and Quantum Materials Center, George Mason University, Fairfax, Virginia 22030, United States;* orcid.org/0000-0003-3848-5632
Reza Zadegan − *Micron School of Materials Science and Engineering and the Computer Science Department, Boise State University, Boise, Idaho 83706, United States; Department of Nanoengineering, The Joint School of Nanoscience and Nanoengineering, North Carolina A&T State University, Greensboro, North Carolina 27401, United States;* orcid.org/0000-0001-9662-7331
Susan Buckhout-White − *Center for Bio/Molecular Science and Engineering, Code 6900, U.S. Naval Research Laboratory, Washington, District of Columbia 20375, United States*
Mario G. Ancona − *Electronic Science and Technology Division, Code 6800, U.S. Naval Research Laboratory, Washington, District of Columbia 20375, United States*
Paul D. Cunningham − *Electronic Science and Technology Division, Code 6800, U.S. Naval Research Laboratory, Washington, District of Columbia 20375, United States;* orcid.org/0000-0002-3602-1503
Joseph S. Melinger − *Electronic Science and Technology Division, Code 6800, U.S. Naval Research Laboratory, Washington, District of Columbia 20375, United States*
Patrick M. Vora − *Department of Physics and Astronomy and Quantum Materials Center, George Mason University, Fairfax, Virginia 22030, United States;* orcid.org/0000-0003-3967-8137
Wan Kuang − *Department of Electrical and Computer Engineering, Boise State University, Boise, Idaho 83706, United States*

Complete contact information is available at: https://pubs.acs.org/10.1021/acsanm.0c00038

Notes

The authors declare no competing financial interest.

■ ACKNOWLEDGMENTS

W.P.K. is thankful for the National Research Council Fellowship through the U.S. Naval Research Laboratory (NRL). The authors appreciatively acknowledge funding from the Office of Naval Research, NRL, and the NRL-Nanosciences Institute. P.M.V. and S.M.O. acknowledge support from the National Science Foundation (NSF) under Grant No. DMR-1748650, the George Mason University (GMU) Quantum Materials Center, and the GMU Presidential Scholars Program.

■ REFERENCES

(1) Wang, R.; Zhang, G.; Liu, H. DNA-Templated Nanofabrication. *Curr. Opin. Colloid Interface Sci.* **2018**, *38*, 88−99.
(2) Bui, H.; Díaz, S. A.; Fontana, J.; Chiriboga, M.; Veneziano, R.; Medintz, I. L. Utilizing the Organizational Power of DNA Scaffolds for New Nanophotonic Applications. *Adv. Opt. Mater.* **2019**, *7*, No. 1900562.
(3) Olejko, L.; Bald, I. FRET Efficiency and Antenna Effect in Multi-Color DNA Origami-Based Light Harvesting Systems. *RSC Adv.* **2017**, *7*, 23924−23934.
(4) Hemmig, E. A.; Creatore, C.; Wünsch, B.; Hecker, L.; Mair, P.; Parker, M. A.; Emmott, S.; Tinnefeld, P.; Keyser, U. F.; Chin, A. W. Programming Light-Harvesting Efficiency Using DNA Origami. *Nano Lett.* **2016**, *16*, 2369−2374.
(5) Kownacki, M.; Langenegger, S. M.; Liu, S.-X.; Häner, R. Integrating DNA Photonic Wires into Light-Harvesting Supramolecular Polymers. *Angew. Chem.* **2019**, *131*, 761−765.
(6) Klein, W. P.; Díaz, S. A.; Chiriboga, M.; Walper, S. A.; Medintz, I. L. Dendrimeric DNA-Based Nanoscaffolded BRET-FRET Optical Encryption Keys. *ACS Appl. Nano Mater* **2019**, *2*, 7459−7465.
(7) Goldman, N.; Bertone, P.; Chen, S.; Dessimoz, C.; LeProust, E. M.; Sipos, B.; Birney, E. Towards Practical, High-Capacity, Low-Maintenance Information Storage in Synthesized DNA. *Nature* **2013**, *494*, 77−80.
(8) Mathur, D.; Medintz, I. L. The Growing Development of DNA Nanostructures for Potential Healthcare-Related Applications. *Adv. Healthc. Mater* **2019**, *8*, No. 1801546.
(9) Ramakrishnan, S.; Schärfen, L.; Hunold, K.; Fricke, S.; Grundmeier, G.; Schlierf, M.; Keller, A.; Krainer, G. Enhancing the Stability of DNA Origami Nanostructures: Staple Strand Redesign Versus Enzymatic Ligation. *Nanoscale* **2019**, *11*, 16270−16276.
(10) Stephanopoulos, N. Strategies for Stabilizing DNA Nanostructures to Biological Conditions. *ChemBioChem* **2019**, *20*, 2191−2197.
(11) Hong, F.; Zhang, F.; Liu, Y.; Yan, H. DNA Origami: Scaffolds for Creating Higher Order Structures. *Chem. Rev.* **2017**, *117*, 12584−12640.
(12) Wagenbauer, K. F.; Sigl, C.; Dietz, H. Gigadalton-Scale Shape-Programmable DNA Assemblies. *Nature* **2017**, *552*, 78−83.
(13) Choi, Y.; Kotthoff, L.; Olejko, L.; Resch-Genger, U.; Bald, I. DNA Origami-Based Förster Resonance Energy-Transfer Nanoarrays and Their Application as Ratiometric Sensors. *ACS Appl. Mater. Interfaces* **2018**, *10*, 23295−23302.
(14) Selnihhin, D.; Sparvath, S. M.; Preus, S.; Birkedal, V.; Andersen, E. S. Multifluorophore DNA Origami Beacon as a Biosensing Platform. *ACS Nano* **2018**, *12*, 5699−5708.
(15) Kato, T.; Kashida, H.; Kishida, H.; Yada, H.; Okamoto, H.; Asanuma, H. Development of a Robust Model System of FRET Using Base Surrogates Tethering Fluorophores for Strict Control of Their Position and Orientation within DNA Duplex. *J. Am. Chem. Soc.* **2013**, *135*, 741−750.
(16) Cunningham, P. D.; Kim, Y. C.; Díaz, S. A.; Buckhout-White, S.; Mathur, D.; Medintz, I. L.; Melinger, J. S. Optical Properties of Vibronically Coupled Cy3 Dimers on DNA Scaffolds. *J. Phys. Chem. B* **2018**, *122*, 5020−5029.
(17) Li, N.; Shang, Y.; Han, Z.; Wang, T.; Wang, Z.-G.; Ding, B. Fabrication of Metal Nanostructures on DNA Templates. *ACS Appl. Mater. Interfaces* **2019**, *11*, 13835−13852.
(18) Brown, C. W., III; Samanta, A.; Díaz, S. A.; Buckhout-White, S.; Walper, S. A.; Goldman, E. R.; Medintz, I. L. Dendrimeric DNA Nanostructures as Scaffolds for Efficient Bidirectional BRET−FRET Cascades. *Adv. Opt. Mater.* **2017**, *5*, No. 1700181.
(19) Klein, W. P.; Schmidt, C. N.; Rapp, B.; Takabayashi, S.; Knowlton, W. B.; Lee, J.; Yurke, B.; Hughes, W. L.; Graugnard, E.; Kuang, W. Multiscaffold DNA Origami Nanoparticle Waveguides. *Nano Lett.* **2013**, *13*, 3850−3856.
(20) Klein, W. P.; Thomsen, R. P.; Turner, K. B.; Walper, S. A.; Vranish, J.; Kjems, J.; Ancona, M. G.; Medintz, I. L. Enhanced Catalysis from Multienzyme Cascades Assembled on a DNA Origami Triangle. *ACS Nano* **2019**, *13*, 13677−13689.
(21) Mathur, D.; Klein, W. P.; Chiriboga, M.; Bui, H.; Oh, E.; Nita, R.; Naciri, J.; Johns, P.; Fontana, J.; Díaz, S. A.; Medintz, I. L. Analyzing Fidelity and Reproducibility of DNA Templated Plasmonic Nanostructures. *Nanoscale* **2019**, *11*, 20693−20706.
(22) Benson, E.; Mohammed, A.; Gardell, J.; Masich, S.; Czeizler, E.; Orponen, P.; Högberg, B. DNA Rendering of Polyhedral Meshes at the Nanoscale. *Nature* **2015**, *523*, 441.
(23) Douglas, S. M.; Marblestone, A. H.; Teerapittayanon, S.; Vazquez, A.; Church, G. M.; Shih, W. M. Rapid Prototyping of 3D DNA-Origami Shapes with CaDNAno. *Nucleic Acids Res.* **2009**, *37*, 5001−5006.

(24) Buckhout-White, S.; Spillmann, C. M.; Algar, W. R.; Khachatrian, A.; Melinger, J. S.; Goldman, E. R.; Ancona, M. G.; Medintz, I. L. Assembling Programmable FRET-Based Photonic Networks Using Designer DNA Scaffolds. *Nat. Commun.* **2014**, *5*, No. 5615.
(25) Spillmann, C. M.; Ancona, M. G.; Buckhout-White, S.; Algar, W. R.; Stewart, M. H.; Susumu, K.; Huston, A. L.; Goldman, E. R.; Medintz, I. L. Achieving Effective Terminal Exciton Delivery in Quantum Dot Antenna-Sensitized Multistep DNA Photonic Wires. *ACS Nano* **2013**, *7*, 7101−7118.
(26) Medintz, I.; Hildebrandt, N. *FRET - Förster Resonance Energy Transfer: From Theory to Applications*; Wiley-VCH Verlag, 2013.
(27) Vyawahare, S.; Eyal, S.; Mathews, K. D.; Quake, S. R. Nanometer-Scale Fluorescence Resonance Optical Waveguides. *Nano Lett.* **2004**, *4*, 1035−1039.
(28) Spillmann, C. M.; Buckhout-White, S.; Oh, E.; Goldman, E. R.; Ancona, M. G.; Medintz, I. L. Extending FRET Cascades on Linear DNA Photonic Wires. *Chem. Commun.* **2014**, *50*, 7246−7249.
(29) Klein, W. P.; Díaz, S. A.; Buckhout-White, S.; Melinger, J. S.; Cunningham, P. D.; Goldman, E. R.; Ancona, M. G.; Kuang, W.; Medintz, I. L. Utilizing HomoFRET to Extend DNA-Scaffolded Photonic Networks and Increase Light-Harvesting Capability. *Adv. Opt. Mater.* **2018**, *6*, No. 1700679.
(30) Díaz, S. A.; Buckhout-White, S.; Ancona, M. G.; Spillmann, C. M.; Goldman, E. R.; Melinger, J. S.; Medintz, I. L. Extending DNA-Based Molecular Photonic Wires with Homogeneous Förster Resonance Energy Transfer. *Adv. Opt. Mater.* **2016**, *4*, 399−412.
(31) Nicoli, F.; Barth, A.; Bae, W.; Neukirchinger, F.; Crevenna, A. H.; Lamb, D. C.; Liedl, T. Directional Photonic Wire Mediated by Homo-Förster Resonance Energy Transfer on a DNA Origami Platform. *ACS Nano* **2017**, *11*, 11264−11272.
(32) Roberti, M. J.; Giordano, L.; Jovin, T. M.; Jares-Erijman, E. A. FRET Imaging by K_t/K_f. *ChemPhysChem* **2011**, *12*, 563−566.
(33) Melo, A. M.; Fedorov, A.; Prieto, M.; Coutinho, A. Exploring Homo-FRET to Quantify the Oligomer Stoichiometry of Membrane-Bound Proteins Involved in a Cooperative Partition Equilibrium. *Phys. Chem. Chem. Phys.* **2014**, *16*, 18105−18117.
(34) Díaz, S. A.; Oliver, S. M.; Hastman, D. A.; Medintz, I. L.; Vora, P. M. Increased Transfer Efficiency from Molecular Photonic Wires on Solid Substrates and Cryogenic Conditions. *J. Phys. Chem. Lett.* **2018**, *9*, 3654−3659.
(35) Dutta, P. K.; Varghese, R.; Nangreave, J.; Lin, S.; Yan, H.; Liu, Y. DNA-Directed Artificial Light-Harvesting Antenna. *J. Am. Chem. Soc.* **2011**, *133*, 11985−11993.
(36) Mathieu, F.; Liao, S.; Kopatsch, J.; Wang, T.; Mao, C.; Seeman, N. C. Six-Helix Bundles Designed from DNA. *Nano Lett.* **2005**, *5*, 661−665.
(37) Cunningham, P. D.; Khachatrian, A.; Buckhout-White, S.; Deschamps, J. R.; Goldman, E. R.; Medintz, I. L.; Melinger, J. S. Resonance Energy Transfer in DNA Duplexes Labeled with Localized Dyes. *J. Phys. Chem. B* **2014**, *118*, 14555−14565.
(38) Schröder, T.; Scheible, M. B.; Steiner, F.; Vogelsang, J.; Tinnefeld, P. Interchromophoric Interactions Determine the Maximum Brightness Density in DNA Origami Structures. *Nano Lett.* **2019**, *19*, 1275−1281.
(39) Huff, J. S.; Davis, P. H.; Christy, A.; Kellis, D. L.; Kandadai, N.; Toa, Z. S. D.; Scholes, G. D.; Yurke, B.; Knowlton, W. B.; Pensack, R. D. DNA-Templated Aggregates of Strongly Coupled Cyanine Dyes: Nonradiative Decay Governs Exciton Lifetimes. *J. Phys. Chem. Lett.* **2019**, *10*, 2386−2392.
(40) Paunovska, K.; Loughrey, D.; Sago, C. D.; Langer, R.; Dahlman, J. E. Using Large Datasets to Understand Nanotechnology. *Adv. Mater.* **2019**, *31*, No. 1902798.
(41) Moroz, P.; Klein, W. P.; Akers, K.; Vore, A.; Kholmicheva, N.; Razgoniaeva, N.; Khon, D.; Díaz, S. A.; Medintz, I. L.; Zamkov, M. Lifting the Spectral Crosstalk in Multifluorophore Assemblies. *J. Phys. Chem. C* **2017**, *121*, 26226−26232.
(42) Li, C.-Y.; Hemmig, E. A.; Kong, J.; Yoo, J.; Hernández-Ainsa, S.; Keyser, U. F.; Aksimentiev, A. Ionic Conductivity, Structural Deformation, and Programmable Anisotropy of DNA Origami in Electric Field. *ACS Nano* **2015**, *9*, 1420−1433.
(43) Bellot, G.; McClintock, M. A.; Lin, C.; Shih, W. M. Recovery of Intact DNA Nanostructures after Agarose Gel-Based Separation. *Nat. Methods* **2011**, *8*, 192−194.
(44) Lakowicz, J. R. *Principles of Fluorescence Spectroscopy*; Springer: New York, 2006.
(45) Dolghih, E.; Roitberg, A. E.; Krause, J. L. Fluorescence Resonance Energy Transfer in Dye-Labeled DNA. *J. Photochem. Photobiol., A* **2007**, *190*, 321−327.
(46) Kashida, H.; Kawai, H.; Maruyama, R.; Kokubo, Y.; Araki, Y.; Wada, T.; Asanuma, H. Quantitative Evaluation of Energy Migration between Identical Chromophores Enabled by Breaking Symmetry. *Commun. Chem.* **2018**, *1*, No. 91.
(47) Hardin, J. C.; Sweet, A. L. Moments of the Time to Absorption in the Random Walk between a Reflecting and an Absorbing Barrier. *SIAM Rev.* **1970**, *12*, 140−142.
(48) Weesakul, B. The Random Walk between a Reflecting and an Absorbing Barrier. *Ann. Math. Stat.* **1961**, *32*, 765−769.
(49) Said, H.; Schüller, V. J.; Eber, F. J.; Wege, C.; Liedl, T.; Richert, C. M1.3 − a Small Scaffold for DNA Origami. *Nanoscale* **2013**, *5*, 284−290.
(50) Green, C. M.; Schutt, K.; Morris, N.; Zadegan, R. M.; Hughes, W. L.; Kuang, W.; Graugnard, E. Metrology of DNA Arrays by Super-Resolution Microscopy. *Nanoscale* **2017**, *9*, 10205−10211.
(51) Strauss, M. T.; Schueder, F.; Haas, D.; Nickels, P. C.; Jungmann, R. Quantifying Absolute Addressability in DNA Origami with Molecular Resolution. *Nat. Commun.* **2018**, *9*, No. 1600.
(52) Gemmill, K. B.; Díaz, S. A.; Blanco-Canosa, J. B.; Deschamps, J. R.; Pons, T.; Liu, H.-W.; Deniz, A.; Melinger, J.; Oh, E.; Susumu, K.; Stewart, M. H.; Hastman, D. A.; North, S. H.; Delehanty, J. B.; Dawson, P. E.; Medintz, I. L. Examining the Polyproline Nanoscopic Ruler in the Context of Quantum Dots. *Chem. Mater.* **2015**, *27*, 6222−6237.
(53) Kalinin, S.; Sisamakis, E.; Magennis, S. W.; Felekyan, S.; Seidel, C. A. M. On the Origin of Broadening of Single-Molecule FRET Efficiency Distributions Beyond Shot Noise Limits. *J. Phys. Chem. B* **2010**, *114*, 6197−6206.
(54) Hellenkamp, B.; Schmid, S.; Doroshenko, O.; Opanasyuk, O.; Kühnemuth, R.; Rezaei Adariani, S.; Ambrose, B.; Aznauryan, M.; Barth, A.; Birkedal, V.; Bowen, M. E.; Chen, H.; Cordes, T.; Eilert, T.; Fijen, C.; Gebhardt, C.; Götz, M.; Gouridis, G.; Gratton, E.; Ha, T.; Hao, P.; Hanke, C. A.; Hartmann, A.; Hendrix, J.; Hildebrandt, L. L.; Hirschfeld, V.; Hohlbein, J.; Hua, B.; Hübner, C. G.; Kallis, E.; Kapanidis, A. N.; Kim, J.-Y.; Krainer, G.; Lamb, D. C.; Lee, N. K.; Lemke, E. A.; Levesque, B.; Levitus, M.; McCann, J. J.; Naredi-Rainer, N.; Nettels, D.; Ngo, T.; Qiu, R.; Robb, N. C.; Röcker, C.; Sanabria, H.; Schlierf, M.; Schröder, T.; Schuler, B.; Seidel, H.; Streit, L.; Thurn, J.; Tinnefeld, P.; Tyagi, S.; Vandenberk, N.; Vera, A. M.; Weninger, K. R.; Wünsch, B.; Yanez-Orozco, I. S.; Michaelis, J.; Seidel, C. A. M.; Craggs, T. D.; Hugel, T. Precision and Accuracy of Single-Molecule FRET Measurements—a Multi-Laboratory Benchmark Study. *Nat. Methods* **2018**, *15*, 669−676.
(55) Sillen, A.; Engelborghs, Y. The Correct Use of "Average" Fluorescence Parameters. *Photochem. Photobiol.* **1998**, *67*, 475−486.
(56) Harvey, B. J.; Levitus, M. Nucleobase-Specific Enhancement of Cy3 Fluorescence. *J. Fluoresc.* **2009**, *19*, 443.
(57) Kretschy, N.; Sack, M.; Somoza, M. M. Sequence-Dependent Fluorescence of Cy3- and Cy5-Labeled Double-Stranded DNA. *Bioconjugate Chem.* **2016**, *27*, 840−848.
(58) Preus, S.; Wilhelmsson, L. M. Advances in Quantitative FRET-Based Methods for Studying Nucleic Acids. *ChemBioChem* **2012**, *13*, 1990−2001.
(59) Netzel, T. L.; Nafisi, K.; Zhao, M.; Lenhard, J. R.; Johnson, I. Base-Content Dependence of Emission Enhancements, Quantum Yields, and Lifetimes for Cyanine Dyes Bound to Double-Strand DNA: Photophysical Properties of Monomeric and Bichromomphoric DNA Stains. *J. Phys. Chem. A.* **1995**, *99*, 17936−17947.
(60) Dimura, M.; Peulen, T. O.; Hanke, C. A.; Prakash, A.; Gohlke, H.; Seidel, C. A. M. Quantitative FRET Studies and Integrative

https://dx.doi.org/10.1021/acsanm.0c00038
ACS Appl. Nano Mater. 2020, 3, 3323−3336

Modeling Unravel the Structure and Dynamics of Biomolecular Systems. *Curr. Opin. Struct. Biol.* **2016**, *40*, 163−185.
(61) Vogel, S. S.; van der Meer, B. W.; Blank, P. S. Estimating the Distance Separating Fluorescent Protein FRET Pairs. *Methods* **2014**, *66*, 131−138.
(62) Melinger, J. S.; Khachatrian, A.; Ancona, M. G.; Buckhout-White, S.; Goldman, E. R.; Spillmann, C. M.; Medintz, I. L.; Cunningham, P. D. FRET from Multiple Pathways in Fluorophore-Labeled DNA. *ACS Photonics* **2016**, *3*, 659−669.
(63) Sindbert, S.; Kalinin, S.; Nguyen, H.; Kienzler, A.; Clima, L.; Bannwarth, W.; Appel, B.; Müller, S.; Seidel, C. A. M. Accurate Distance Determination of Nucleic Acids Via Förster Resonance Energy Transfer: Implications of Dye Linker Length and Rigidity. *J. Am. Chem. Soc.* **2011**, *133*, 2463−2480.
(64) Breiman, L. Random Forests. *Mach. Learn.* **2001**, *45*, 5−32.
(65) Salim, B.; Pria Knj, J. M.; Alagappan, M.; Kandaswamy, A. In *Fabrication of Poly (Methyl Methacrylate) and Poly(vinyl alcohol) Thin Film Capacitors on Flexible Substrates*, IOP Conference Series: Materials Science and Engineering, 2015.
(66) Cipolloni, M.; Fresch, B.; Occhiuto, I.; Rukin, P.; Komarova, K. G.; Cecconello, A.; Willner, I.; Levine, R. D.; Remacle, F.; Collini, E. Coherent Electronic and Nuclear Dynamics in a Rhodamine Heterodimer−DNA Supramolecular Complex. *Phys. Chem. Chem. Phys.* **2017**, *19*, 23043−23051.
(67) Kawski, A.; Kubicki, A.; Kukliński, B.; Gryczyński, I. Unusual Absorption and Fluorescence Properties of 1,6-Diphenyl- 1,3,5-Hexatriene in Poly(Vinyl Alcohol) Film. *J. Photochem. Photobiol., A* **1993**, *71*, 161−167.
(68) Aramendia, P. F.; Negri, R. M.; Roman, E. S. Temperature Dependence of Fluorescence and Photoisomerization in Symmetric Carbocyanines. Influence of Medium Viscosity and Molecular Structure. *J. Phys. Chem. B.* **1994**, *98*, 3165−3173.
(69) Winiger, C. B.; Langenegger, S. M.; Calzaferri, G.; Häner, R. Formation of Two Homo-Chromophoric H-Aggregates in DNA-Assembled Alternating Dye Stacks. *Angew. Chem., Int. Ed.* **2015**, *54*, 3643−3647.
(70) Pan, K.; Bricker, W. P.; Ratanalert, S.; Bathe, M. Structure and Conformational Dynamics of Scaffolded DNA Origami Nanoparticles. *Nucleic Acids Res.* **2017**, *45*, 6284−6298.
(71) Pan, K.; Boulais, E.; Yang, L.; Bathe, M. Structure-Based Model for Light-Harvesting Properties of Nucleic Acid Nanostructures. *Nucleic Acids Res.* **2014**, *42*, 2159−2170.
(72) Azcárate, J. C.; Díaz, S. A.; Fauerbach, J. A.; Gillanders, F.; Rubert, A. A.; Jares-Erijman, E. A.; Jovin, T. M.; Fonticelli, M. H. ESIPT and FRET Probes for Monitoring Nanoparticle Polymer Coating Stability. *Nanoscale* **2017**, *9*, 8647−8656.
(73) Cunningham, P. D.; Bricker, W. P.; Díaz, S. A.; Medintz, I. L.; Bathe, M.; Melinger, J. S. Optical Determination of the Electronic Coupling and Intercalation Geometry of Thiazole Orange Homodimer in DNA. *J. Chem. Phys.* **2017**, *147*, No. 055101.
(74) Pons, T.; Medintz, I. L.; Wang, X.; English, D. S.; Mattoussi, H. Solution-Phase Single Quantum Dot Fluorescence Resonance Energy Transfer. *J. Am. Chem. Soc.* **2006**, *128*, 15324−15331.
(75) Wager, S.; Hastie, T.; Efron, B. Confidence Intervals for Random Forests: The Jackknife and the Infinitesimal Jackknife. *J. Mach. Learn. Res.* **2014**, *15*, 1625−1651.
(76) Bilal, M.; Oh, E.; Liu, R.; Breger, J. C.; Medintz, I. L.; Cohen, Y. Bayesian Network Resource for Meta-Analysis: Cellular Toxicity of Quantum Dots. *Small* **2019**, *15*, No. 1900510.

https://dx.doi.org/10.1021/acsanm.0c00038
ACS Appl. Nano Mater. 2020, 3, 3323−3336